coatings

MDPI

Article

Enhancing Short-Term Plasticity by Inserting a Thin TiO_2 Layer in WO_x-Based Resistive Switching Memory

Hyojong Cho and Sungjun Kim *

Division of Electronics and Electrical Engineering, Dongguk University, Seoul 04620, Korea; chj9102@dgu.ac.kr
* Correspondence: sungjun@dongguk.edu

Received: 2 September 2020; Accepted: 21 September 2020; Published: 22 September 2020

Abstract: In this work, we emulate biological synaptic properties such as long-term plasticity (LTP) and short-term plasticity (STP) in an artificial synaptic device with a $TiN/TiO_2/WO_x/Pt$ structure. The graded WO_x layer with oxygen vacancies is confirmed via X-ray photoelectron spectroscopy (XPS) analysis. The control $TiN/WO_x/Pt$ device shows filamentary switching with abrupt set and gradual reset processes in DC sweep mode. The $TiN/WO_x/Pt$ device is vulnerable to set stuck because of negative set behavior, as verified by both DC sweep and pulse modes. The $TiN/WO_x/Pt$ device has good retention and can mimic long-term memory (LTM), including potentiation and depression, given repeated pulses. On the other hand, $TiN/TiO_2/WO_x/Pt$ devices show non-filamentary type switching that is suitable for fine conductance modulation. Potentiation and depression are demonstrated in the TiN/TiO_2 (2 nm)/WO_x/Pt device with moderate conductance decay by application of identical repeated pulses. Short-term memory (STM) is demonstrated by varying the interval time of pulse inputs for the TiN/TiO_2 (6 nm)/WO_x/Pt device with a quick decay in conductance.

Keywords: short-term plasticity; in-memory computing; resistive switching; X-ray photoelectron spectroscopy

1. Introduction

Resistive switching memory (RRAM) has long been studied as a type of high-density storage that can replace NAND flash in academia and industry [1–6]. Although there have been many advances in terms of endurance [7], retention [8], and low-power operation [9,10], it has not achieved the good reproducibility, repeatability, and low variability required by industry. As NAND flash was developed with a 3D vertical structure, X-point array type RRAM was no longer able to compete at cost per bit [11]. However, RRAM is a strong candidate for storage class memory (SCM) applications, where it can serve as a buffer to overcome the latency difference between DRAM as working memory and NAND flash as storage memory [12]. Moreover, the analog switching behavior of RRAM can create multiple conductance levels, which can be applied to synaptic devices for neuromorphic systems on the hardware level [13]. The von Neumann structure is a built-in computing model that has a typical three-level structure consisting of a main memory device, a central processing device, and an input/output device; it executes commands sequentially, resulting in a data bottleneck. A neuromorphic chip can process large amounts of data in parallel and in an energy efficient manner. With the development of artificial intelligence (AI), big data, and machine learning, the field has responded to the necessity for computation and processing of massive amounts of data efficiently and with low energy usage [14].

Synaptic devices such as RRAM [15–19] and phase change memory (PRAM) [20,21] can reduce the burden of computation compared to a graphics processing unit (GPU)-based deep learning framework by employing weight updating by matrix multiplication. Moreover, a two-terminal RRAM device can maximize memory density compared to three-terminal devices. Until now, synaptic behaviors like potentiation, depression, spike-timing dependent plasticity (STDP) [22], and short-term plasticity (STP) have been emulated in several materials such as metal oxides [23], metal nitrides [24], and organic materials [25]. STP in a synaptic device is suitable for temporary data processing such as reservoir computing. Recently, temporal information processing was demonstrated by using a memristor device [26]. The train cost can be reduced when using reservoir computing compared to the traditional recurrent neural network.

Non-filamentary type switching is more suitable for fine weight updates compared to filamentary type switching when implementing synaptic behaviors [27]. Metal oxides such as WO_x [28–33], TiO_x [34–36], and TaO_x [37,38] show both filamentary and non-filamentary switching depending on the process conditions, film thickness, combination of electrodes, and switching operation.

In this work, we characterize the synaptic behaviors of TiO_2/WO_x-based RRAM devices for neuromorphic systems. First, the deposition of TiO_2 and the oxygen vacancies in graded WO_x film are confirmed by XPS analysis. Filamentary and non-filamentary characteristics are distinguished through I–V characteristics in TiN/WO_x/Pt and TiN/TiO_2/WO_x/Pt devices. Set stuck because of negative set behavior in the single-layer device is verified. STP is enhanced by introduction of a thin TiO_2 layer between the top electrode and WO_x layer. Moreover, we experimentally demonstrate STP in the TiN/TiO_2 (6 nm)/WO_x/Pt device with a fast decay in conductance.

2. Materials and Methods

The TiN/WO_x/Pt device was fabricated as follows. A 100-nm-thick Pt bottom electrode was deposited by e-beam evaporation on a SiO_2/Si wafer. A 10-nm-thick WO_x layer was deposited by pulsed DC sputtering. The W target was reactive with Ar (8 sccm) and O_2 (12 sccm) at a sputtering pressure of 1 mTorr. Then, 2-nm-thick and 6-nm-thick TiO_2 films were deposited by atomic layer deposition (ALD, NCD, Dajeon, South Korea) using precursors of titanium isopropoxide (TTIP) and H_2O at a chamber temperature of 200 °C for bilayer samples. Then, a 100-nm-thick TiN top electrode was deposited by DC sputtering and patterned by a shadow mask containing circular patterns with a diameter of 100 µm. All electrical properties including DC and transient characteristics were measured using a Keithley 4200-SCS semiconductor parameter analyzer ultrafast module (Keithley, Solon, OH, USA) and in pulse mode using a 4225-PMU ultrafast module (Keithley, Solon, OH, USA). All measurements were performed at room temperature and ambient atmospheric pressure. A bias was applied to the TiN top electrode while the Pt bottom electrode was grounded. XPS depth analysis was conducted with a Nexsa (ThermoFisher Scientific, Waltham, MA, USA) with a Microfocus monochromatic X-ray source (Al-Kα (1486.6 eV)), a sputter source (Ar^+), an ion energy of 2 kV, and a beam size of 50 µm.

3. Results and Discussion

XPS was used to analyze the chemical compositions of the TiO_2 (6 nm)/WO_x (10 nm)/Pt stack in the bilayer device. Figure 1a–c show the XPS spectra of Ti 2p, W 4f, and Pt 4f, respectively, at different depths. For the Ti 2p core level spectra on the surface before etching, the binding energies of two peaks are centered at 459.2 and 465 eV, corresponding to Ti $2p_{3/2}$ and Ti $2p_{1/2}$ in Figure 1a [39]. This indicates that the ALD TiO_2 layer is close to the appropriate stoichiometry. The peak positions of Ti 2p are shifted left between 4 and 8 s due to the $TiWO_x$ interlayer between TiO_2 and WO_x. Fully oxidized WO_3 is detected by reactive sputtering of the W target at 0 s given the weak-intensity peaks of W $4f_{7/2}$ and W $4f_{5/2}$ that are located at ~36.05 and ~38.05 eV, respectively, in Figure 1b [40]. The WO_3 layer should be detected at 0 s considering the scan range of X-ray because the thickness of the TiO_2 layer is just 6 nm. Oxygen-deficient WO_{3-x} film is dominant after an etching time of 4 s, when the peaks of W $4f_{7/2}$ and W $4f_{5/2}$ are located from 31.7 to 32.9 eV and 34 to 35.1 eV, respectively [40]. Two peaks (W $4f_{7/2}$ and W $4f_{5/2}$) of unoxidized W are seen during the initial deposition process, which are located at ~31.5 and 33.5 eV, respectively. Initially, there are oxygen vacancies in graded WO_x film, the presence of which is favorable to resistive switching. The Pt bottom electrode is dominantly detected after an etching time of 12 s, when 4$f_{7/2}$ and 4$f_{5/2}$ are centered at ~71.3 and ~74.6 eV, respectively, in Figure 1c [41].

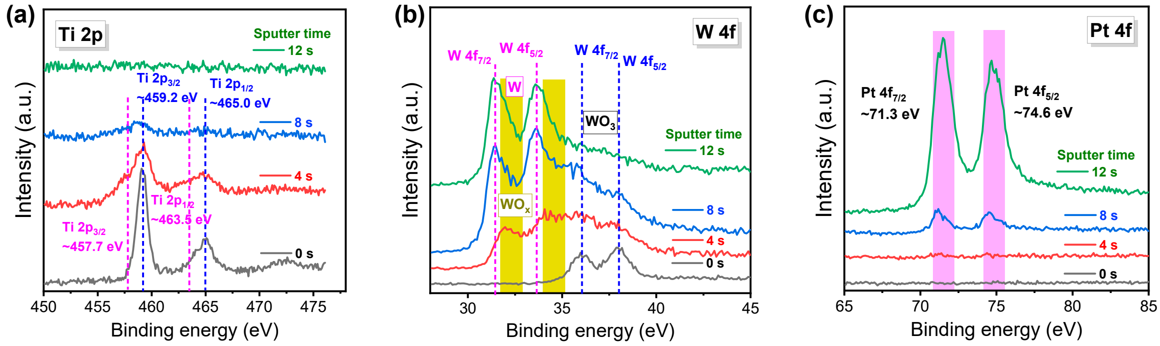

Figure 1. XPS spectra of (**a**) Ti 2p, (**b**) W 4f, and (**c**) Pt 4f in TiO_2 (6 nm)/WO_x (10 nm)/Pt stack.

Figure 2 shows typical DC I–V curves of three TiN/WO_x/Pt devices. High current operation is inevitable during the set (high-resistance state (HRS) to low-resistance state (LRS)) and reset (LRS to HRS) processes due to initially high current flow. WO_x-based RRAM devices show both filamentary and non-filamentary switching depending on device size, film thickness, operating condition, electrode type, and presence and type of insulating layer [28–33]. Filamentary switching was clearly observed in high current operation in the Pt/WO_x/W device [42]. The set transition with abrupt current jump occurs under the excessive defect condition. This switching occurs because of the formation and rupture of a localized conducting filament. The TiN electrode as a reactive metal can form a TiON interfacial layer, which provides better resistive switching when a positive bias is applied on the TiN electrode [43]. On the other hand, a gradual resistance change is seen in the TiN/TiO_2/WO_x/Pt devices without electroforming in Figure 2. This current hysteresis is due to the movement of oxygen ions/vacancies in the WO_x and the TiO_2 layers. When a negative bias is applied, the oxygen ions move from two insulating layers toward the Pt bottom electrode, increasing the number of oxygen vacancies and the conductance. Conversely, when a positive bias is applied, the oxygen vacancies generated during the set process move toward the TiN top electrode and the conductance decreases. Here, since the TiO_2 layer retains some insulating properties, the current can be lowered when the thickness of the TiO_2 layer increases from 2 to 6 nm.

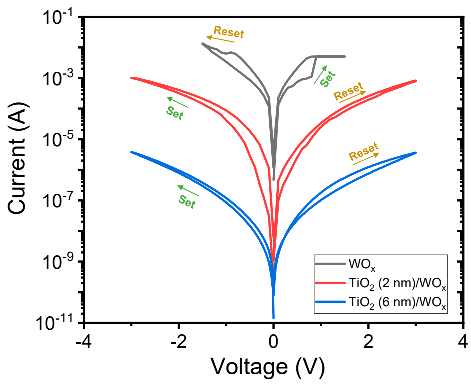

Figure 2. Typical I–V characteristics of three devices (TiN/WO_x/Pt device, TiN/TiO_2 (2 nm)/WO_x/Pt device, TiN/TiO_2 (6 nm)/WO_x/Pt devices).

Figure 3a shows the DC endurance cycle of the TiN/WO_x/Pt device. The read voltage of −0.9 V is used to distinguish between the two states. The reset stop voltage (V_{STOP}) is increased from −1.5 to −1.8 V to enlarge the ON/OFF ratio. However, an increase in sweeping voltage (−1.9 V) leads to reset switching failure, as shown in Figure 3b. The LRS that occurs once the device enters set stuck cannot return to HRS, which is one of the main reasons for endurance failure. Set stuck from negative set behavior occurs due to the parasitic filaments from the electrode [44]. Therefore, the device should be carefully controlled within a negative set margin during the gradual reset process. On the other hand, TiN/TiO_2/WO_x/Pt devices have a higher sweep range, from −3 to 3 V, compared to the TiN/WO_x/Pt device, which has no immunity against set stuck by negative set process, as shown in Figure 3. However, it is difficult to obtain repeatable and uniform resistive switching properties from cycle to cycle due to poor retention characteristics.

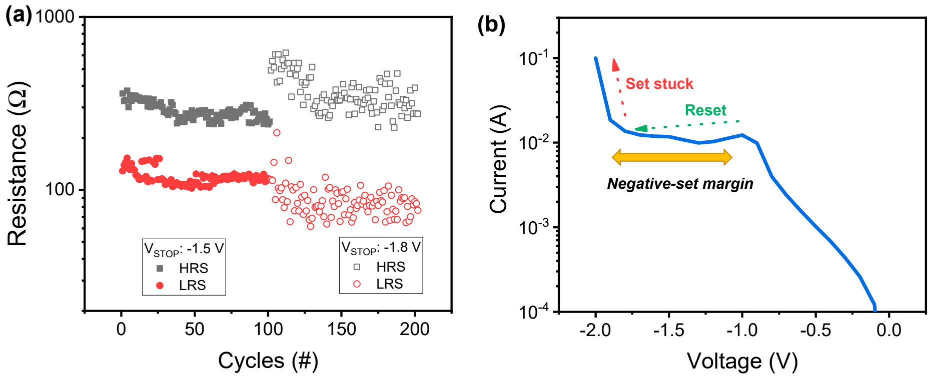

Figure 3. (**a**) DC endurance of the TiN/WO_x/Pt device according to reset stop voltage. (**b**) Reset switching failure by large voltage sweep.

Moreover, the set and reset and negative set processes are conducted by pulse. The overshoot current effect is minimized by a triangular waveform that gradually and slowly increases the rising and falling time of the applied voltage in the main pulse. The increased current is confirmed by a read voltage of 0.2 V after the peak voltage reaches 2.2 V for the set process in Figure 4a. Similarly, decreased current is observed after the peak voltage reaches −1.56 V for the reset process in Figure 4b. On the other hand, the increased current is monitored after the peak voltage reaches −1.72 V for set stuck from negative set behavior in Figure 4c.

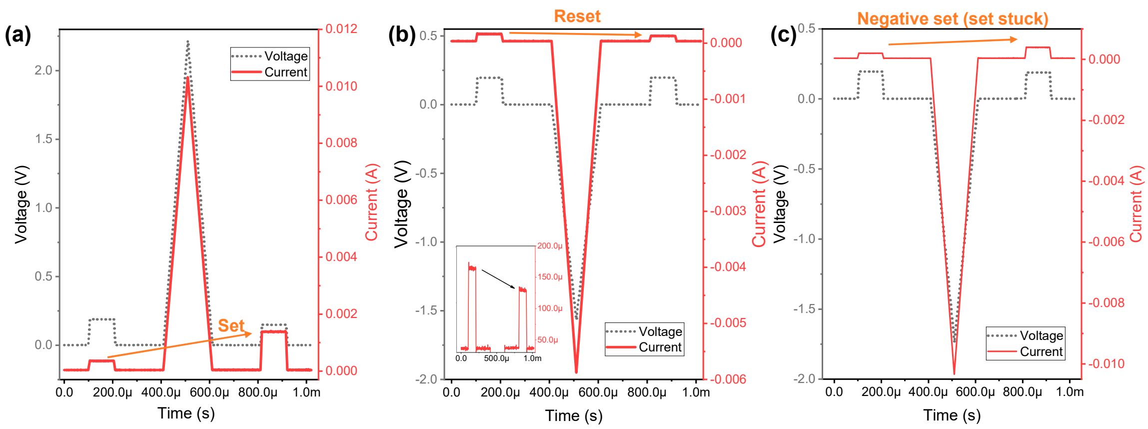

Figure 4. (**a**) Set, (**b**) reset, and (**c**) set stuck by pulse operation mode.

Figure 5 shows the drift of normalized conductance, defined as the ratio between the conductance at a given time (G) and conductance at time zero (G_0), as a function of time for the TiN/WO_x/Pt device, TiN/TiO_2 (2 nm)/WO_x/Pt device, and TiN/TiO_2 (6 nm)/WO_x/Pt device. The conductance is extracted from the current at a read pulse voltage of 0.3 V after the set process. The TiN/WO_x/Pt device, which follows a filamentary model, shows slow conductance decay with only 4% retention loss for 4000 s. Once formed, large conducting filaments do not change significantly over time. On the other hand, the TiN/TiO_2 (2 nm)/WO_x/Pt and TiN/TiO_2 (6 nm)/WO_x/Pt devices show much larger conductance decays of 30.7% and 67.2%, respectively. The poor retention properties indicate that the TiN/TiO_2/WO_x/Pt device follows non-filamentary type switching driven by the movement of oxygen ions/vacancies. Oxygen vacancies, which are temporarily increased by the electric field, can easily recombine with oxygen ions in the vicinity, which results in substantial loss of retention. This property is especially suitable for STP in a neuromorphic system.

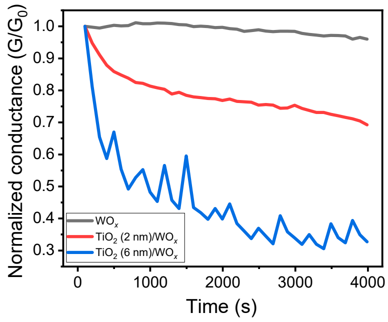

Figure 5. Drift characteristics of normalized conductance decay in the TiN/WO_x/Pt device, TiN/TiO_2 (2 nm)/WO_x/Pt device, and TiN/TiO_2 (6 nm)/WO_x/Pt device.

Figure 6a,b show three consecutive potentiation and depression curves in the TiN/WO_x/Pt and TiN/TiO_2 (2 nm)/WO_x/Pt devices, respectively. For potentiation, incremental increases in voltage (0.82 to 0.88125 V) are used to implement multiple conductance states for TiN/WO_x/Pt. Note that a large conductance could change at any given time, representing the abrupt transition during the set process, when repeated identical pulses accumulate in a synaptic device. Moreover, highly linear conductance update is achieved, as shown in Figure 6a. On the other hand, for depression, an identical pulse can cause progressive conductance update because of the gradual switching that occurs during the reset process. For the TiN/TiO_2 (2 nm)/WO_x/Pt device with non-filamentary switching, nonlinear conductance updates are obtained with repeated identical pulse inputs, as shown in Figure 6b. For potentiation and depression, increasing the number of pulses to 100 after two potentiation/depression cycles of 50 pulses each can change the dynamic range even more. On the other hand, the TiN/TiO_2 (6 nm)/WO_x/Pt device is suitable for STP because of its poor retention property.

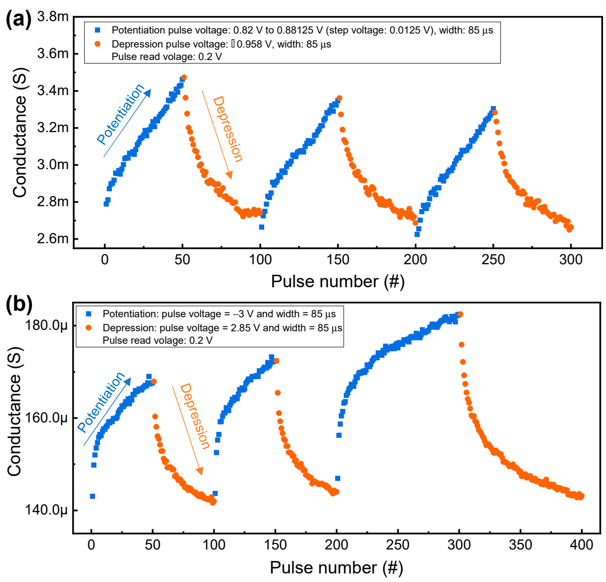

Figure 6. Potentiation and depression characteristics. (**a**) Incremental pulse amplitude increases and identical pulses cause potentiation in the TiN/WO_x/Pt device. (**b**) Identical pulse conditions for the TiN/TiO_2 (2 nm)/WO_x/Pt device.

Figure 7 shows the potentiation and depression caused by changes in the interval time of pulse inputs. Potentiation is obtained when 20 pulses with an amplitude of 8 V, width of 200 µs, and interval time of 100 µs are applied to the device. However, the current significantly decreases after an interval time of 40 ms, indicating that depression occurs.

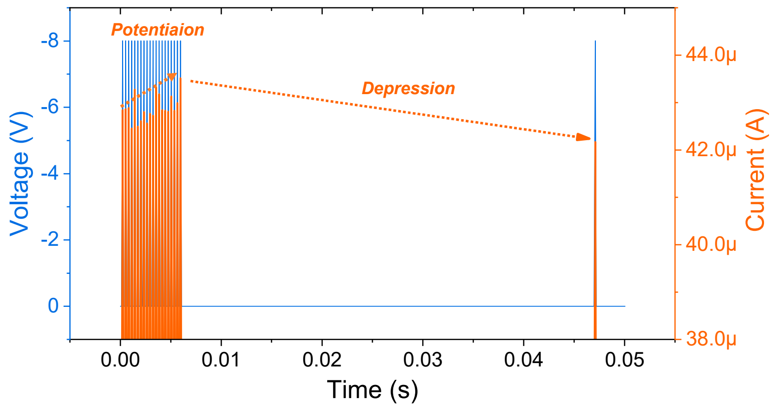

Figure 7. Potentiation and depression characteristics caused by controlling pulse interval time in the TiN/TiO_2 (6 nm)/WO_x/Pt device.

4. Conclusions

We demonstrate synaptic behaviors such as LTP and STP in $TiN/WO_x/Pt$ and $TiN/TiO_2/WO_x/Pt$ devices. XPS analysis confirms the non-uniform oxygen gradient in the WO_x layer. The $TiN/WO_x/Pt$ device following filamentary type switching should be carefully controlled under DC sweep and pulse modes during reset switching to avoid set stuck. Insertion of TiO_2 between the TiN and WO_x layers causes the device to work with non-filamentary type switching with weak data retention. Potentiation and depression are mimicked by repeated pulses in the $TiN/WO_x/Pt$ and TiN/TiO_2 (2 nm)/WO_x/Pt devices. Finally, STM is demonstrated by simply controlling the interval time between pulse inputs for the TiN/TiO_2 (6 nm)/WO_x/Pt device with poor retention.

Author Contributions: H.C. conducted the electrical measurements and wrote the manuscript; S.K. designed the experiment concept and supervised the study. All authors have read and agreed to the published version of the manuscript.

Funding: This work was supported in part by the National Research Foundation of Korea (NRF), grant funded by the Korean government (MSIP) under grant 2018R1C1B5046454.

Conflicts of Interest: The authors declare that they have no competing interests.

References

1. Chang, S.H.; Lee, S.B.; Jeon, D.Y.; Park, S.J.; Kim, G.T.; Yang, S.M.; Chae, S.C.; Yoo, H.K.; Kang, B.S.; Lee, M.-J.; et al. Oxide double-layer nanocrossbar for ultrahigh-density bipolar resistive memory. *Adv. Mater.* **2011**, *23*, 4063–4067. [CrossRef]
2. Jo, S.H.; Kim, K.-H.; Lu, W. High-density crossbar arrays based on a Si memristive system. *Nano Lett.* **2009**, *9*, 870–874. [CrossRef]
3. Lee, M.-J.; Lee, C.B.; Lee, D.; Lee, S.R.; Chang, M.; Hur, J.H.; Kim, Y.-B.; Kim, C.-J.; Seo, D.H.; Chung, U.-I.; et al. A fast, high-endurance and scalable non-volatile memory device made from asymmetric Ta_2O_{5-x}/TaO_{2-x} bilayer structures. *Nat. Mater.* **2011**, *10*, 625–630. [CrossRef] [PubMed]
4. Waser, R.; Dittmann, R.; Staikov, G.; Szot, K. Redox-based resistive switching memories nanoionic mechanisms, prospects, and challenges. *Adv. Mater.* **2009**, *21*, 2632–2663. [CrossRef]
5. Mikhaylov, A.; Belov, A.; Korolev, D.; Antonov, I.; Kotomina, V.; Kotina, A.; Gryaznov, E.; Sharapov, A.; Koryazhkina, M.; Kryukov, R.; et al. Multilayer metal-oxide memristive device with stabilized resistive switching. *Adv. Mater. Technol.* **2020**, *5*, 1900607. [CrossRef]

6. Upadhyay, N.K.; Sun, W.; Lin, P.; Joshi, S.; Midya, R.; Zhang, X.; Wang, Z.; Jiang, H.; Yoon, J.H.; Rao, M.; et al. A memristor with low switching current and voltage for 1S1R integration and array operation. *Adv. Electron. Mater.* **2020**, *6*, 1901411. [CrossRef]
7. Huang, X.-D.; Li, Y.; Li, H.-Y.; Xue, K.-H.; Wang, X.; Miao, X.-S. Forming-Free, Fast, Uniform, and high endurance resistive switching from cryogenic to high temperatures in W/AlO_x/Al_2O_3/Pt bilayer memristor. *IEEE Electron Device Lett.* **2020**, *41*, 549–552. [CrossRef]
8. Cai, L.; Chen, W.; Zhao, Y.; Liu, X.; Kang, J.; Zhang, X.; Huang, P. Insight into effects of oxygen reservoir layer and operation schemes on data retention of HfO_2-based RRAM. *IEEE Trans. Electron Devices* **2019**, *66*, 3822–3827. [CrossRef]
9. Kim, S.; Jung, S.; Kim, M.-H.; Chen, Y.-C.; Chang, Y.-F.; Ryoo, K.-C.; Cho, S.; Lee, J.-H.; Park, B.-G. Scaling effect on silicon nitride memristor with highly doped Si substrate. *Small* **2018**, *14*, 1704062. [CrossRef]
10. Kim, S.; Jung, S.; Kim, M.-H.; Cho, S.; Park, B.-G. Resistive switching characteristics of Si_3N_4-based resistive-switching random-access memory cell with tunnel barrier for high density integration and low-power applications. *Appl. Phys. Lett.* **2015**, *106*, 212016. [CrossRef]
11. Kim, Y.; Yun, J.-G.; Park, S.H.; Kim, W.; Seo, J.Y.; Kang, M.; Ryoo, K.-C.; Oh, J.-H.; Lee, J.-H.; Shin, H.; et al. Three-dimensional NAND flash architecture design based on single-crystalline STacked Array. *IEEE Trans. Electron Devices* **2012**, *59*, 35–45. [CrossRef]
12. Fong, S.W.; Neumann, C.M.; Wong, H.-S.P. Phase-change memory—towards a storage-class memory. *IEEE Trans. Electron Devices* **2017**, *64*, 4374–4385. [CrossRef]
13. Chang, T.; Jo, S.-H.; Lu, W. Short-term memory to long-term memory transition in a nanoscale memristor. *ACS Nano* **2011**, *5*, 7669–7676. [CrossRef] [PubMed]
14. Boahen, K.A. Point-to-point connectivity between neuromorphic chips using address events. *IEEE Trans. Circuits Syst. II Analog Digit. Signal Process.* **2000**, *47*, 416–434. [CrossRef]
15. Yu, S.; Gao, B.; Fang, Z.; Yu, H.; Kang, J.; Wong, H.-S.P. A low energy oxide-based electronic synaptic device for neuromorphic visual systems with tolerance to device variation. *Adv. Mater.* **2013**, *25*, 1774–1779. [CrossRef] [PubMed]
16. Kim, S.; Chen, J.; Chen, Y.-C.; Kim, M.-H.; Kim, H.; Kwon, M.-W.; Hwang, S.; Ismail, M.; Li, Y.; Miao, X.-S.; et al. Neuronal dynamics in HfO_x/AlO_y-based homeothermic synaptic memristors with low-power and homogeneous resistive switching. *Nanoscale* **2019**, *11*, 237–245. [CrossRef] [PubMed]
17. Ielmini, D. Brain-inspired computing with resistive switching memory (RRAM): Devices, synapses and neural networks. *Microelectron. Eng.* **2018**, *190*, 44–53. [CrossRef]
18. Woo, J.; Moon, K.; Song, J.; Lee, S.; Kwak, M.; Park, J.; Hwang, H. Improved synaptic behavior under identical pulses using AlO_x/HfO_2 bilayer RRAM array for neuromorphic systems. *IEEE Electron Device Lett.* **2016**, *37*, 994–997. [CrossRef]
19. Kim, S.; Kim, H.; Hwang, S.; Kim, M.-H.; Chang, Y.-F.; Park, B.-G. Analog synaptic behavior of a silicon nitride memristor. *ACS Appl. Mater. Interfaces* **2017**, *9*, 40420–40427. [CrossRef]
20. Li, Y.; Zhong, Y.; Xu, L.; Zhang, J.; Xu, X.; Sun, H.; Miao, X. Ultrafast synaptic events in a chalcogenide memristor. *Sci. Rep.* **2013**, *3*, 1619. [CrossRef]
21. Eryilmaz, S.B.; Kuzum, D.; Jeyasingh, R.; Kim, S.; Brightsky, M.; Lam, C.; Wong, H.-S.P. Brain-like associative learning using a nanoscale non-volatile phase change synaptic device array. *Front. Neurosci.* **2014**, *8*, 205. [CrossRef] [PubMed]
22. Ambrogio, S.; Balatti, S.; Nardi, F.; Facchinetti, S.; Ielmini, D. Spike-timing dependent plasticity in a transistor-selected resistive switching memory. *Nanotechnology* **2013**, *24*, 384012. [CrossRef] [PubMed]
23. Yu, S.; Wu, Y.; Jeyasingh, R.; Kuzum, D.; Wong, H.-S.P. An electronic synapse device based on metal oxide resistive switching memory for neuromorphic computation. *IEEE Trans. Electron Devices* **2011**, *58*, 2729–2737. [CrossRef]
24. Zhu, W.; Li, J. Synaptic learning and forgetting behavior in Ag/AlN/Al memristor with O_2 annealing effect. *IEEE Access* **2019**, *7*, 163358–163364. [CrossRef]
25. Minnekhanov, A.A.; Shvetsov, B.S.; Martyshov, M.M.; Nikiruy, K.E.; Kukueva, E.V.; Presnyakov, M.Y.; Forsh, P.A.; Rylkov, V.V.; Erokhin, V.V.; Demin, V.A.; et al. On the resistive switching mechanism of parylene-based memristive devices. *Org. Electron.* **2019**, *74*, 89–95. [CrossRef]
26. Du, C.; Cai, F.; Zidan, M.A.; Ma, W.; Lee, S.H.; Lu, W.D. Reservoir computing using dynamic memristors for temporal information processing. *Nat. Comm.* **2017**, *8*, 2204. [CrossRef]

27. Moon, K.; Lim, S.; Park, J.; Sung, C.; Oh, S.; Woo, J.; Lee, J.; Hwang, H. RRAM-based synapse devices for neuromorphic systems. *Faraday Discuss.* **2019**, *213*, 421–451. [CrossRef]
28. Chen, W.-J.; Cheng, C.-H.; Lin, P.-E.; Tseng, Y.-T.; Chang, T.-C.; Chen, J.-S. Analog resistive switching and synaptic functions in WO_x/TaO_x bilayer through redox-induced trap-controlled conduction. *ACS Appl. Electron. Mater.* **2019**, *1*, 2422–2430. [CrossRef]
29. Kim, J.; Inamdar, A.I.; Jo, Y.; Woo, H.; Cho, S.; Pawar, S.M.; Kim, H.S.; Im, H. Effect of electronegativity on bipolar resistive switching in a WO_3-based asymmetric capacitor structure. *ACS Appl. Mater. Interfaces* **2016**, *8*, 9499–9505. [CrossRef]
30. Won, S.; Lee, S.Y.; Park, J.; Seo, H. Forming-less and non-volatile resistive switching in WO_x by oxygen vacancy control at interfaces. *Sci. Rep.* **2017**, *7*, 10186. [CrossRef]
31. Syu, Y.-E.; Chang, T.-C.; Tsai, T.-M.; Chang, G.-W.; Chang, K.-C.; Tai, Y.-H.; Tsai, M.-J.; Wang, Y.-L.; Sze, S.M. Silicon introduced effect on resistive switching characteristics of WO_x thin films. *Appl. Phys. Lett.* **2012**, *100*, 022904. [CrossRef]
32. Yang, R.; Terabe, K.; Yao, Y.; Tsuruoka, T.; Hasegawa, T.; Gimzewski, J.K.; Aono, M. Synaptic plasticity and memory functions achieved in a WO_{3-x}-based nanoionics device by using the principle of atomic switch operation. *Nanotechnology* **2013**, *24*, 384003. [CrossRef] [PubMed]
33. Tsai, T.-L.; Lin, Y.-H.; Tseng, T.-Y. Resistive Switching Characteristics of WO_3/ZrO_2 structure with forming-free, self-compliance, and submicroampere current operation. *IEEE Electron Device Lett.* **2015**, *36*, 675–677. [CrossRef]
34. Bousoulas, P.; Asenov, P.; Karageorgiou, I.; Sakellaropoulos, D.; Stathopoulos, S.; Tsoukalas, D. Engineering amorphous-crystalline interfaces in TiO_{2-x}/TiO_{2-y}-based bilayer structures for enhanced resistive switching and synaptic properties. *J. Appl. Phys.* **2016**, *120*, 154501. [CrossRef]
35. Zhao, B.; Xiao, M.; Zhou, Y.N. Synaptic learning behavior of a TiO_2 nanowire memristor. *Nanotechnology* **2019**, *30*, 425202. [CrossRef]
36. Kim, T.-H.; Kim, M.-H.; Bang, S.; Lee, D.K.; Kim, S.; Cho, S.; Park, B.-G. Fabrication and characterization of TiO_x memristor for synaptic device application. *IEEE Trans. Nanotechnol.* **2020**, *19*, 475–480.
37. Li, S.-J.; Dong, B.-Y.; Wang, B.; Li, Y.; Sun, H.-J.; He, Y.-H.; Xu, N.; Miao, X.-S. Alleviating conductance nonlinearity via pulse shape designs in TaO_x memristive synapses. *IEEE Trans. Electron Devices* **2019**, *66*, 810–813. [CrossRef]
38. Liu, S.; Li, K.; Sun, Y.; Zhu, X.; Li, Z.; Song, B.; Liu, H.; Li, Q. A TaO_x-based electronic synapse with high precision for neuromorphic computing. *IEEE Access* **2019**, *7*, 184700–184706. [CrossRef]
39. Hernández-Arriaga, H.; López-Luna, E.; Martínez-Guerra, E.; Turrubiartes, M.M.; Rodríguez, A.G.; Vidal, M.A. Growth of HfO_2/TiO_2 nanolaminates by atomic layer deposition and HfO_2-TiO_2 by atomic partial layer deposition. *J. Appl. Phys.* **2017**, *121*, 064302. [CrossRef]
40. Alov, N.V. XPS study of MoO_3 and WO_3 oxide surface modification by low-energy Ar^+ ion bombardment. *Phys. Status Solidi C.* **2015**, *12*, 263–266. [CrossRef]
41. Matin, M.A.; Lee, E.; Kim, H.; Yoon, W.-S.; Kwon, Y.-U. Rational syntheses of core-shell Fe@(PtRu) nanoparticle electrocatalysts for the methanol oxidation reaction with complete suppression of CO-poisoning and highly enhanced activity. *J. Mater. Chem. A* **2015**, *3*, 17154–17164. [CrossRef]
42. Biju, K.P.; Liu, X.; Siddik, M.; Kim, S.; Shin, J.; Kim, I.; Ignatiev, A.; Hwang, H. Resistive switching characteristics and mechanism of thermally grown WO_x thin films. *J. Appl. Phys.* **2011**, *110*, 064505. [CrossRef]
43. Rahmani, M.K.; Ismail, M.; Mahata, C.; Kim, S. Effect of interlayer on resistive switching properties of SnO_2-based memristor for synaptic application. *Res. Phy.* **2020**, *18*, 103325. [CrossRef]
44. Park, W.Y.; Ju, W.; Ko, Y.S.; Kim, S.G.; Ha, T.J.; Lee, J.Y.; Park, Y.T.; Kim, K.W.; Lee, J.C.; Lee, J.H.; et al. Improvement of sensing margin and reset switching fail of RRAM. *Solid State Electron.* **2019**, *156*, 87–91. [CrossRef]

© 2020 by the authors. Licensee MDPI, Basel, Switzerland. This article is an open access article distributed under the terms and conditions of the Creative Commons Attribution (CC BY) license (http://creativecommons.org/licenses/by/4.0/).